科学通报 2023 年 第 68 卷 第 20 期: 2642 ~ 2647
快 讯
《中国科学》杂志社
SCIENCE CHINA PRESS

熔/流体迁移与2022年泸定*Ms* 6.8地震

董兴朋[1], 杨顶辉[2*], 蒙伟娟[2]

1. 中国地震局地质研究所, 北京 100029;
2. 清华大学数学科学系, 北京 100084
* 联系人, E-mail: ydh@tsinghua.edu.cn

2023-01-05 收稿, 2023-02-12 修回, 2023-03-25 接受, 2023-03-28 网络版发表
国家自然科学基金(U1839206, 42004077)和中国博士后科学基金(2020M670285)资助

摘要 2022年9月5日, 鲜水河断裂带东南末端发生泸定*Ms* 6.8级地震, 造成严重的人员伤亡和财产损失. 为深入探究该地震构造背景和孕震机理, 利用全波形反演方法获得了震源区及周边高精度地震波速度、径向各向异性和泊松比结构. 研究表明, 泸定地震发生在低波速异常区边缘, 在其下方存在显著的低S波速、负径向各向异性(V_{SH}<V_{SV})和高泊松比异常区, 此热-流变结构异常区的形成可能与深部地壳和上地幔流体(包括部分熔融)有关, 这些熔/流体沿倾斜的Moho面和/或壳内断裂向上迁移, 引起中上地壳孕震层的弱化和应力集中, 进而导致地震发生, 表明深部熔/流体迁移在泸定地震孕育和破裂过程中发挥着重要作用.

关键词 泸定地震, 熔/流体迁移, 全波形反演, 孕震机理

受印度板块持续向北推挤和西侧坚硬塔里木克拉通的阻挡, 青藏高原物质沿内部大型走滑断裂带大规模向东"逃逸"[1]. 作为巴颜喀拉地块与川滇菱形块体的边界, 鲜水河断裂带在协调藏东地壳物质挤出与块体旋转运动方面起着重要作用. 此外, 鲜水河断裂带还是中国大陆内部地震活动性最强的断裂带之一, 1700年以来发生7级以上强震8次, 6.0~6.9级地震18次, 几乎整个断裂带沿线都有强震发生[2]. 2022年9月5日发生的泸定*Ms* 6.8级地震主发震断层为鲜水河断裂带南东段的磨西断裂, 已经造成了严重的人员伤亡和重大的经济损失. 在历史上, 磨西断裂曾于1786年发生过7¾级破坏性强震, 诱发周缘山体滑坡, 堵塞大渡河, 造成严重的水患. 因此, 研究泸定地震及其周边区域深部结构、热-流变状态和变形特征将有助于加深对该区域强震孕育和发生机理的认识.

地震层析成像是获取地球深部结构最重要的工具之一, 许多学者已利用背景噪声成像和射线层析成像等方法开展了该地区地壳和上地幔尺度速度结构的研究, 取得了一些有意义的成果, 加深了人们对该区域深部结构的认识[3~5]. 然而, 前人研究多限于单一类型地震波速(如P或S波)结构, 难以提供深部地壳介质的流变性和变形特征等关键信息. 事实上, 强震孕育的时间尺度可长达数百年乃至上千年, 它不是简单的弹性行为, 而是涉及复杂的流变过程. 因此, 获得整个青藏高原东缘区域(特别是其内部大型断裂带)高精度和多参数三维壳幔结构图像(如速度、各向异性和泊松比等), 探讨区域内强震(如泸定地震)发震构造背景和深部流变结构特征, 是当前研究的热点和重要方向. 要达到此目的, 需要发展一种能最大化利用地震波形信号中所有有用信息(包括走时和振幅)的方法. 全波形层析成像能同时利用地震记录中的相位和振幅信息来约束地下结构, 分辨率最高可达最短波长的一半, 优于其他传统的层析成像方法, 是一种非常合适的选择[6].

近年来, 随着计算机性能的提升和现代数值方法(如谱元法)的应用, 全波形层析成像已逐渐应用于区域乃至全球尺度壳幔结构的研究中. 相较于传统的射线类层析成像方法, 它有以下优势: (1) 数值求解3D复杂地球模型中精确的理论地震图; (2) 考虑了射线路径之外的3D敏感核; (3) 可充分利用完整的波形信息(包括P波、S波、反射波和转换波以及面波等)进行反演. 针对泸定地震深部构造背景和变形特征, 本研究基于

引用格式: 董兴朋, 杨顶辉, 蒙伟娟. 熔/流体迁移与2022年泸定*Ms* 6.8地震. 科学通报, 2023, 68: 2642–2647
Dong X P, Yang D H, Meng W J. Melt/fluid migration and the 2022 Luding *Ms* 6.8 earthquake (in Chinese). Chin Sci Bull, 2023, 68: 2642–2647, doi: 10.1360/TB-2023-0015

青藏高原东缘密集的区域地震事件和台网分布，利用全波形成像获得了该区域震源区及其周边高精度的地壳和上地幔顶部S波速度、径向各向异性和泊松比结构图像.

利用100个区域地震事件和118个固定地震台站接收到的高质量地震三分量波形数据(图1)，同时反演纵波速度(V_P)、水平极化(V_{SH})和垂直极化(V_{SV})剪切波速度. 由于剪切波(S波)速度与地球内部材料的剪切模量紧密相关，与纵波速度相比，它对岩石中的流体成分更敏感，能更好地反映地壳深处介质的热-流变状态，因此本文主要展示震源区及周边S波速度($V_S=\sqrt{\frac{2V_{SV}^2+V_{SH}^2}{3}}$)的分布. 此外，我们还给出了泊松比($\upsilon$)和径向各向异性($\xi=\frac{V_{SH}-V_{SV}}{V_S}$)的分布图像，以进一步约束震源区及其下方介质流变特性(如流体含量和部分熔融程度等)与深部变形机制.

泸定M_S 6.8级地震发生后，中国地震台网中心测定的震源深度参考值为16 km，故我们给出了研究区在16 km深度处S波的水平切片图(图1(b)). 可以看到，青藏高原内部各块体，包括巴颜喀拉块体、羌塘块体和川西北次级块体都表现为明显的低S波速异常，而四川盆地和扬子块体则表现为明显的高S波速特征. 泸定地震震中位于鲜水河断裂带东南末端，大致位于鲜水河断裂带、龙门山断裂带、安宁河-则木河断裂带和丽江-小金河这4条大型断裂带的交汇处(图1(a)). 在S波切片图上可明显看到它处于低波速、相对柔软的川滇菱形块体和高波速、坚硬的四川盆地交界处(图1(b)), 其成因与青藏块体内部物质在遇到四川盆地阻挡后沿鲜水河断裂带向东南运移有关. 为了检验成像结果的可靠性, 我们进行了恢复性测试. 在初始模型的泸定地震震源区附近设置小的SV波低速扰动异常，然后利用伴随方法计算相应的水平极化剪切波(horizontally polarized shear wave, SH wave)和垂直极化剪切波(vertically polarized shear wave, SV wave)的Fréchet敏感核(图2)，可以看到, SV波的Fréchet敏感核(图2(c))很好地恢

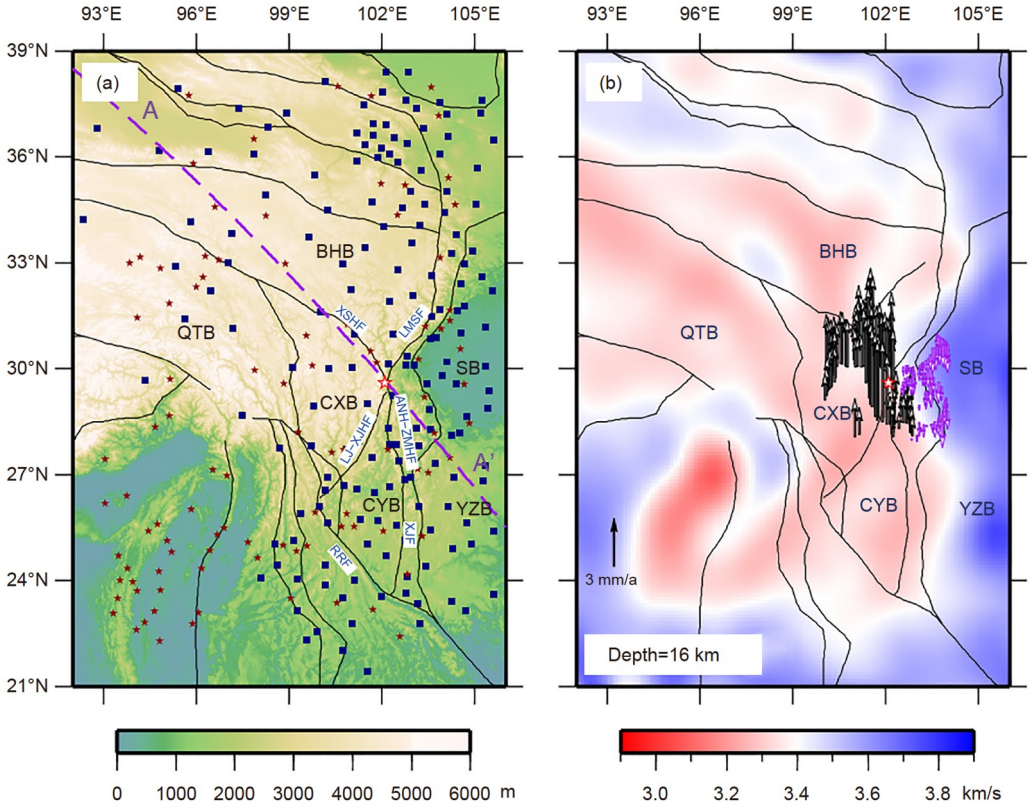

图 1 研究区地质构造和S波成像结果. (a) 反演中用到的区域地震事件(五角星)和台站(正方形)分布图. (b) 16 km深度S波速度分布. 白红色五角星代表2022年M_S 6.8泸定地震; 箭头代表水准垂直运动大小(相对ITRF2008参考框架). SB: 四川盆地; BHB: 巴颜喀拉块体; QTB: 羌塘块体; CXB: 川西北次级块体; CYB: 滇中次级块体; YZB: 扬子块体; LMSF: 龙门山断裂带; XSHF: 鲜水河断裂带; LJ-XJHF: 丽江-小金河断裂带; ANH-ZMHF: 安宁河-则木河断裂带; XJF: 小江断裂带; RRF: 红河断裂带

Figure 1 Geological setting of study area and imaging results of S-wave velocity. (a) The seismic events (stars) and stations (squares) involved in the inversion. (b) Map view of S-wave velocity at 16 km depth. White star denotes 2022 Luding M_S 6.8 earthquake; the arrows indicate the vertical movements inferred from precise leveling data (relative to ITRF2008 reference framework). SB: Sichuan basin; BHB: Bayan Har block; QTB: Qiangtang block; CXB: Chuanxibei sub-block; CYB: Central Yunnan sub-block; YZB: Yangtze block; LMSF: Longmenshan fault; XSHF: Xianshuihe fault; LJ-XJHF: Lijiang-Xiaojinhe fault; ANH-ZMHF: Anninghe-Zemuhe fault; XJF: Xiaojiang fault; RRF: Red River fault

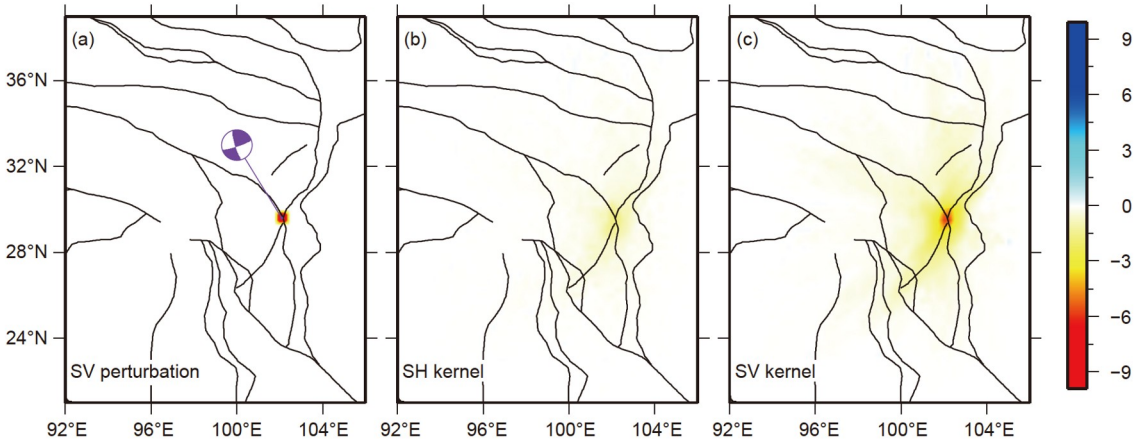

图 2 泸定*Ms* 6.8地震震源区异常体恢复测试. (a) 真实SV波速度扰动; (b) SH波Fréchet敏感核; (c) SV波Fréchet敏感核. 颜色棒单位为1.0×10^{-12} s^2/m^4

Figure 2 The recovery test of anomaly body around the focal region of the Luding *Ms* 6.8 earthquake. (a) True SV velocity perturbation; (b) Fréchet kernel of SH wave; (c) Fréchet kernel of SV wave. The unit of the colorbar is 1.0×10^{-12} s^2/m^4

复了异常区的形状, 且V_{SH}与V_{SV}之间的Tradeoff可以忽略不计. 由于在全波形成像中Fréchet敏感核代表了模型的更新方向, 所以这一测试结果表明我们的反演结果是可靠的(图2).

鲜水河断裂带是现今东亚大陆活动性最强的大型断裂带之一, 南与安宁河-则木河断裂带相接, 全球定位系统(Global Positioning System, GPS)研究显示, 其南东段左旋走滑速率为9~10 mm/a, 地壳运动变形强烈[7]. 震源机制解显示泸定*Ms* 6.8地震为走滑型(www.globalcmt.org; 图2(a)), 表明其主要是由川滇块体与巴颜喀拉块体之间的差异运动造成的. 然而, 该地震是否仅受水平作用控制, 其成因与地壳深部介质结构与变形等是否有关仍需要进一步厘清. 为此, 我们给出了沿29.6°N和102.1°E的两个横跨泸定地震震源区的垂向S波速、径向各向异性和泊松比切片图. 图3和4(a)~(d)显示, 泸定地震震源区下方存在显著低S波速(–6%)和高泊松比异常(0.30), 深度范围从约15 km到上地幔顶部. 一般而言, 地壳岩石的地震波速和泊松比取决于物质成分、温度、压力和流体含量等因素[8]. 研究表明, 岩石泊松比随流体含量或部分熔融程度增加而变大, 而流体含量(包含部分熔融)增加又会导致S波速度显著降低[9]. 因而, 低S波速和高泊

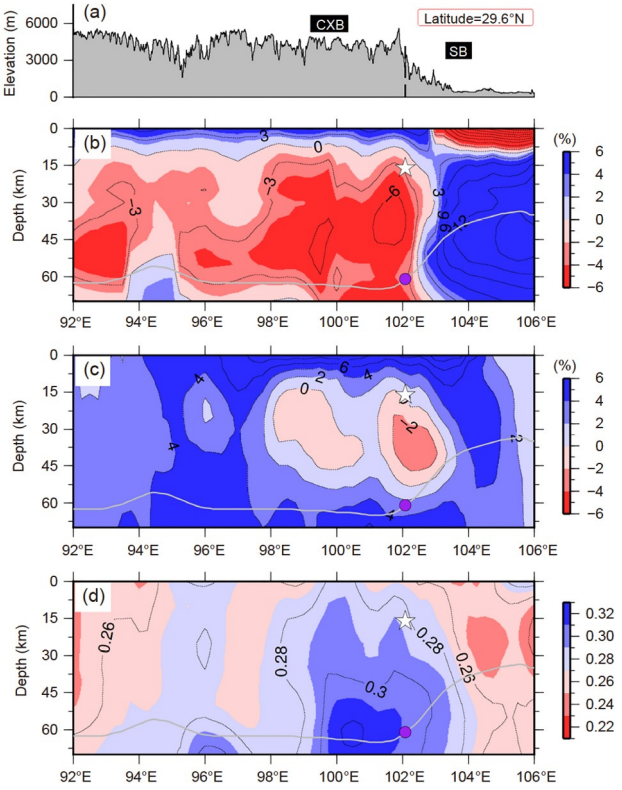

图 3 沿北纬29.6°的地表高程(a)、S波速度扰动(b)、径向各向异性(c)和泊松比(d)垂向切片图. 白色五角星代表泸定地震; 灰线代表Moho面埋深, 其由反演模型中S波速度为4.1 km/s对应的深度估算而来; 紫色圆圈对应与泸定地震震中相对的Moho面位置; 速度参考值为每个深度层的平均值

Figure 3 Vertical cross section with surface elevation (a), S-wave velocity perturbation (b), radial anisotropy (c), and Poisson's ratio (d) along 29.6°N. The white star denotes Luding earthquake; the gray line represents the Moho, which is derived from the depth corresponding to the S-wave velocity of 4.1 km/s; the purple circle corresponds to the position of Moho relative to the Luding earthquake; the reference speed is the average value of each depth layer

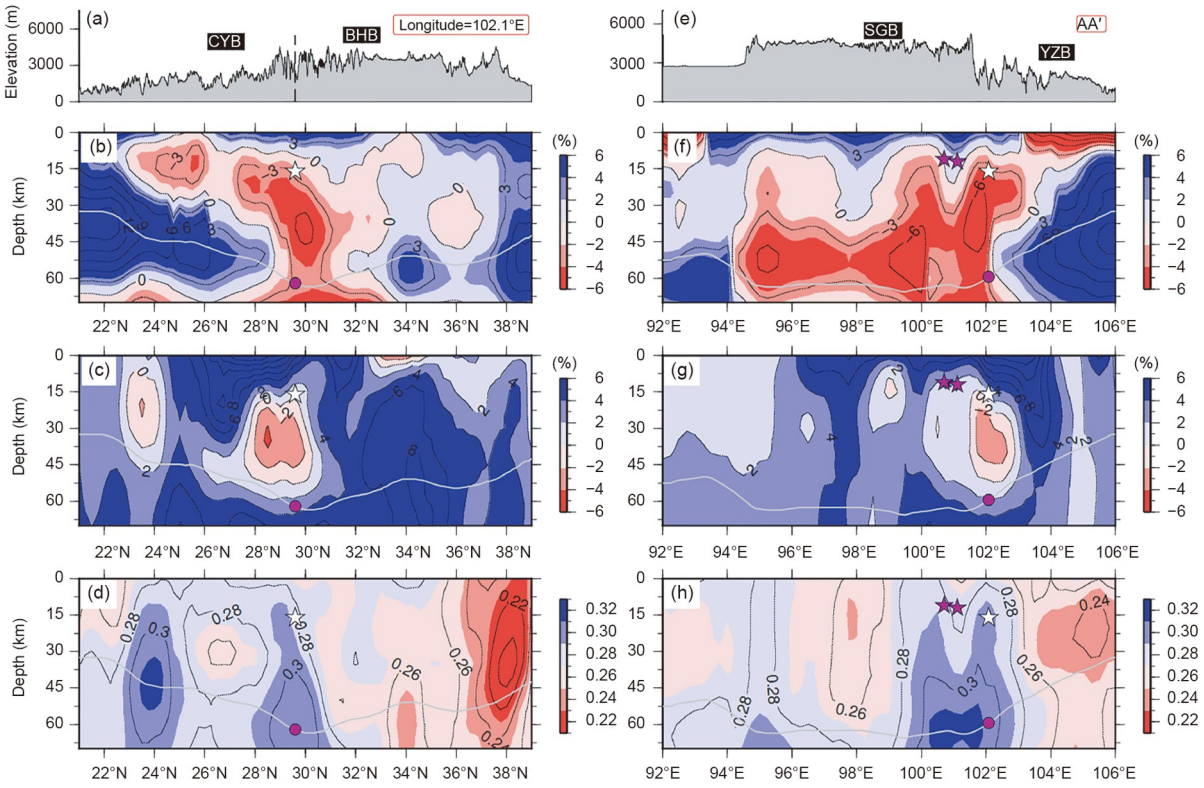

图 4 沿102.1°E和AA′剖面的地表高程(a, e)、S波速度扰动(b, f)、径向各向异性(c, g)和泊松比(d, h)垂向切片图. 白色五角星代表泸定地震; 紫色五角星代表沿鲜水河断裂带发生的两次历史强震; 灰线代表Moho面埋深, 其由反演模型中S波速度为4.1 km/s对应的深度估算得来; 紫色圆圈对应与泸定地震震中相对的Moho面位置; 速度参考值为每个深度层的平均值

Figure 4 Vertical cross section with surface elevation (a, e), S-wave velocity perturbation (b, f), radial anisotropy (c, g), and Poisson's ratio (d, h) along 102.1°E and AA′ profiles. The white star denotes Luding earthquake and the purple stars denote two historical large earthquakes occurred in Xianshuihe fault; the gray line represents the Moho, which is derived from the depth corresponding to the S-wave velocity of 4.1 km/s; the purple circle corresponds to the position of Moho relative to the Luding earthquake; the reference speed is the average value of each depth layer

松比特征表明, 该异常区可能与流体(包含部分熔融)或岩浆房有关[10,11]. 鉴于该震源区附近没有火山活动, 所以该异常区可能代表了深部流体的存在. 径向各向异性结果(图3(c)和4(c))显示, 震源区下方介质水平极化的SH波速低于垂直极化的SV波速(V_{SH}<V_{SV}), 由于中下地壳岩石的各向异性与黑云母等矿物的晶格优势排列方向有关[12,13], 联合该区低S波速结构, 反映了地壳深部弱物质的向上流动. 此外, Hao等人[14]研究表明, 泸定地震震中附近存在显著的垂向运动(相对ITRF2008参考框架), 其水准垂直运动幅度达~6 mm/a, 与我们前述的深部地壳弱物质向上流动一致.

基于反演结果, 采用V_s=4.1 km/s来估算研究区内Moho面埋深, 这是地震层析成像中常用的一种估算Moho面埋深的手段, 其结果与接收函数方法获得的指示速度或物性变化的Moho面深度可能存在一定偏差, 但总体趋势一致[15,16]. 泸定地震下方Moho面变化剧烈, 处于从巨厚的高原地壳(约60 km)向周围坚硬地块的正常地壳厚度过渡带的转折点上, Moho面埋深在经过泸定地震下方后开始逐渐抬升(图3和4), 加之地壳底部低速区与上地幔顶部的低速区相连通, 暗示该处深部岩石圈地幔尚未达到重力均衡. 综上所述, 我们认为, 高原中下地壳弱物质在向东流动时受到阻挡, 使得其在泸定地震下方堆积, 这些物质在高温高压下处于部分熔融状态或富含流体, 而来自上地幔顶部的热侵蚀作用也会导致熔/流体向上侵入, 这两者共同作用造成了泸定地震震源区下方的低流变强度异常区的形成. 该异常区熔/流体沿倾斜的Moho面和/或壳内断裂向上迁移, 显著增加中上地壳孕震层的孔隙流体压力, 并大幅降低断层的摩擦断裂强度与破裂临界条件, 而这些受熔/流体侵入的孕震层弱部位又相对容易积累应力, 从而导致了地震在此部位孕育和发生. 为进一步探讨鲜水河断裂带强震的发震背景, 我们沿AA′剖面给出了该断裂带历史上两次震级大于6.7级强震震源区周边的速度扰动、径向各向异性和泊松比垂向切片图(图4(e)~(h)). 可以看到, 尽管这两次强震同泸定地震一样位于低S波速和高泊松比异常区的边缘, 但它们下方却显示了正径向各向异性特征(V_{SH}>V_{SV}), 表明其成因机制可能与泸定地震

不同.

本文基于密集地震台网资料, 利用全波形成像方法获得了泸定震源区及周边高分辨率S波速度、径向各向异性和泊松比结构. 震源区东西两侧S波速度结构存在显著横向差异, 其下方存在低S波速和高泊松比异常区, 暗示流体(部分熔融)存在. 该低速和高泊松比异常区延伸至上地幔顶部, 表明该处深部地幔热物质仍在向上运移与调整. 震源区下方倾斜抬升的Moho面和/或地壳中断裂的存在, 为熔/流体向上运移起通道作用. 这些深部熔/流体迁移至中上地壳孕震层, 弱化了断层强度, 使得孕震断层易于破裂, 进而引发大地震.

致谢 感谢中国地震局地球物理研究所国家测震台网数据备份中心(http://www.seisdmc.ac.cn/)为本研究提供波形数据.

参考文献

1 Tapponnier P, Xu Z Q, Roger F, et al. Oblique stepwise rise and growth of the Tibet Plateau. Science, 2001, 294: 1671–1677

2 Zhang P Z, Wang M, Gan W J, et al. Slip rates along major active faults from GPS measurements and constraints on contemporary continental tectonics (in Chinese). Earth Sci Front, 2003, 10(Suppl): 81–92 [张培震, 王敏, 甘卫军, 等. GPS观测的活动断裂滑动速率及其对现今大陆动力作用的制约. 地学前缘, 2003, 10(Suppl): 81–92]

3 Yao H, Beghein C, van der Hilst R D. Surface wave array tomography in SE Tibet from ambient seismic noise and two-station analysis—II. Crustal and upper-mantle structure. Geophys J Int, 2008, 173: 205–219

4 Huang Z, Wang P, Xu M, et al. Mantle structure and dynamics beneath SE Tibet revealed by new seismic images. Earth Planet Sci Lett, 2015, 411: 100–111

5 Zhang F X, Wu Q J, Ding Z F. A P-wave velocity study beneath the eastern region of Tibetan Plateau and its implication for plateau growth (in Chinese). Chin Sci Bull, 2018, 63: 1949–1961 [张风雪, 吴庆举, 丁志峰. 青藏高原东部P波速度结构及其对高原隆升的启示. 科学通报, 2018, 63: 1949–1961]

6 Virieux J, Operto S. An overview of full-waveform inversion in exploration geophysics. Geophysics, 2009, 74: WCC1–WCC26

7 Wang M, Shen Z K. Present-day crustal deformation of continental China derived from GPS and its tectonic implications. J Geophys Res Solid Earth, 2020, 125: e2019JB018774

8 Zhao D, Kanamori H, Negishi H, et al. Tomography of the source area of the 1995 Kobe Earthquake: Evidence for fluids at the hypocenter? Science, 1996, 274: 1891–1894

9 Watanabe T. Effects of water and melt on seismic velocities and their application to characterization of seismic reflectors. Geophys Res Lett, 1993, 20: 2933–2936

10 Huang J L, Zhao D P. Three-dimensional P-wave velocity minor structure and inner structural enviroment bred by strong shock of the capital circle area (in Chinese). Chin Sci Bull (Chin Ver), 2005, 50: 348–355 [黄金莉, 赵大鹏. 首都圈地区地壳三维P波速度细结构与强震孕育的深部构造环境. 科学通报, 2005, 50: 348–355]

11 Wang Z, Wang J, Yang X. The role of fluids in the 2008 *M*s 8.0 Wenchuan earthquake, China. J Geophys Res Solid Earth, 2020, 126: e2020JB019959

12 Weiss T, Siegesmund S, Rabbel W, et al. Seismic velocities and anisotropy of the lower continental crust: A review. Pure Appl Geophys, 1999, 156: 97–122

13 Shapiro N, Ritzwoller M, Molnar P, et al. Thinning and flow of Tibetan crust constrained by seismic anisotropy. Science, 2004, 305: 233–236

14 Hao M, Wang Q, Shen Z, et al. Present day crustal vertical movement inferred from precise leveling data in eastern margin of Tibetan Plateau. Tectonophysics, 2014, 632: 281–292

15 Bao X, Song X, Li J. High-resolution lithospheric structure beneath mainland of China from ambient noise and earthquake surface-wave tomography. Earth Planet Sci Lett, 2015, 417: 132–141

16 Dong X, Yang D, Niu F. Passive adjoint tomography of the crustal and upper mantle beneath eastern Tibet with a W2-norm misfit function. Geophys Res Lett, 2019, 46: 12986–12995

Summary for “熔/流体迁移与2022年泸定*M*s 6.8地震”

Melt/fluid migration and the 2022 Luding *M*s 6.8 earthquake

Xingpeng Dong[1], Dinghui Yang[2*] & Weijuan Meng[2]

[1] *Institute of Geology, China Earthquake Administration, Beijing 100029, China;*
[2] *Department of Mathematical Sciences, Tsinghua University, Beijing 100084, China*
* Corresponding author, E-mail: ydh@tsinghua.edu.cn

The main seismogenic fault of the 2022 Luding *M*s 6.8 earthquake is the Moxi fault in the southeast section of the Xianshuihe fault zone, which has caused serious casualties and heavy economic losses. Historically, a destructive earthquake of magnitude 7¾ occurred on the Moxi fault in 1786, which caused landslides around the area to block the Dadu River and caused serious flooding. Therefore, studying the deep structure, thermal-rheological state and deformation characteristics of the Luding earthquake and its surrounding areas will help to deepen the understanding of the preparation and occurrence mechanism of large earthquakes in this region. The time scale of large earthquakes can be as long as hundreds of years or even thousands of years. It is not a simple elastic behavior, but involves a complex rheological process. Therefore, obtaining high-resolution and multi-parameter three-dimensional (3D) images of crust-mantle structure (such as velocity, anisotropy, Poisson’s ratio, etc.) of the eastern Tibetan Plateau and discussing the seismogenic tectonic background of large earthquakes in this region are the current hotspots and important directions. To achieve this goal, it is necessary to develop a method that can maximize the use of all useful information (including travel time and amplitude) in seismic waveform signals. Full waveform inversion can simultaneously use phase and amplitude information in seismic records to constrain subsurface structures, with a resolution up to half of the shortest wavelength, which is superior to other traditional tomography methods and is a very suitable choice.

In this study, we use the full waveform inversion method to obtain high-resolution seismic wave velocity, radial anisotropy and Poisson’s ratio structures around the source area of Luding earthquake. In order to verify the reliability of the imaging results, we carried out a recovery test. A small low-velocity perturbation of SV wave is placed near the source area in the initial model and then the Fréchet sensitive kernels of the corresponding SH wave and SV wave are calculated by using the adjoint method. The results suggest that the Fréchet kernel pattern of SV wave is generally consistent with the shape of anomaly body and the tradeoff between V_{SH} and V_{SV} can be ignored. Since the Fréchet kernel indicates the update direction of the model in full waveform inversion, the recovery test demonstrates that our imaging results are reliable. The focal mechanism solution shows that the Luding *M*s 6.8 earthquake is a strike-slip type (www.globalcmt.org), indicating that it is mainly controlled by the differential motion between the Sichuan-Yunan block and the Bayan Har block. However, whether the earthquake was only controlled by horizontal motion still need to be further clarified. For this reason, we give the vertical profiles of the S-wave velocity perturbation, radial anisotropy and Poisson’s ratio along 29.6°N and 102.1°E across the focal area of the Luding earthquake. The results show that the Luding earthquake occurred at the edge of the low-velocity perturbation. There is an anomaly region of low S-wave velocity, negative radial anisotropy ($V_{SH}<V_{SV}$) and high Poisson’s ratio just below the source area of Luding earthquake. The formation of this region may be related to the fluids (including partial melting) within the deep crust and upper mantle. These melts/fluids probably migrate upward along the inclined Moho and/or intracrustal faults, causing the weakening and stress concentration of the seismogenic layer in the middle and upper crust, and leading to the occurrence of earthquakes. Our tomographic results indicate that melt/fluid migration might play an important role in the initiation and rupture of the Luding earthquake.

Luding earthquake, melt/fluid migration, full waveform inversion, seismogenic mechanism

doi: 10.1360/TB-2023-0015